



# Performance of Nano-Electromechanical Systems as Nanoparticle Position Sensors

Ezgi Orhan<sup>1</sup>, Mert Yuksel<sup>1</sup>, Atakan B. Ari<sup>1</sup>, Cenk Yanik<sup>2</sup>, Utku Hatipoglu<sup>1</sup>, Ahmet Murat Yağci<sup>3</sup> and M. Selim Hanay<sup>1,4\*</sup>

<sup>1</sup> Department of Mechanical Engineering, Bilkent University, Ankara, Turkey, <sup>2</sup> SUNUM Sabanci University Nanotechnology Research and Application Center, Istanbul, Turkey, <sup>3</sup> METU MEMS Center, Ankara, Turkey, <sup>4</sup> UNAM – Institute of Material Science, Bilkent University, Ankara, Turkey

## OPEN ACCESS

### Edited by:

Silvan Schmid,  
Vienna University of  
Technology, Austria

### Reviewed by:

Stephen M. Heinrich,  
Marquette University, United States  
Chingfu Tsou,  
Feng Chia University, Taiwan

### \*Correspondence:

M. Selim Hanay  
selimhanay@bilkent.edu.tr

### Specialty section:

This article was submitted to  
Micro- and Nanoelectromechanical  
Systems,  
a section of the journal  
Frontiers in Mechanical Engineering

**Received:** 14 February 2020

**Accepted:** 12 May 2020

**Published:** 10 June 2020

### Citation:

Orhan E, Yuksel M, Ari AB, Yanik C, Hatipoglu U, Yağci AM and Hanay MS (2020) Performance of Nano-Electromechanical Systems as Nanoparticle Position Sensors. *Front. Mech. Eng.* 6:37. doi: 10.3389/fmech.2020.00037

Nanoelectromechanical systems (NEMS) have been utilized as sensitive mass sensors in many applications such as single cell characterization, volatile organic biomarker detection and single molecule mass spectrometry. Using the frequency shift detection, mass of single analytes can be resolved. Mass detection sensitivity can be further improved by accurate measurement of the position, unlocking extra capabilities in nanoscale positioning and manipulation applications. Here, we studied the position sensing performance of two-mode NEMS resonators during detection of single 20 nm gold nanoparticles (GNPs). By recording the position of each particle with frequency shift sensing, the position detection accuracy was evaluated for different beam models and the results are validated by SEM imaging our results indicate that the position sensing accuracy, and therefore the mass sensing accuracy, of nanomechanical resonators depends critically on the use of appropriate beam models.

**Keywords:** NEMS, MEMS, position sensing, nanomanipulation, inertial imaging

## INTRODUCTION

The potential of mass sensing with NEMS devices was recognized in the early 2000s (Ekinci et al., 2004a,b; Ilic et al., 2004). Mass resolution at the zeptogram level was demonstrated a few years later (Yang et al., 2006) with top-down NEMS devices. Meanwhile, bottom-up NEMS devices have also been used in significant demonstrations such as obtaining atomic mass through shot noise statistics (Jensen et al., 2008), detecting single molecules (Chiu et al., 2008; Lassagne et al., 2008), and eventually reaching yoctogram-level resolution (Chaste et al., 2012). In these studies, the analyte has been modeled as a soft particle with a fixed stiffness (Tamayo et al., 2006; Park et al., 2010; Malvar et al., 2016). As a result, the frequency shifts obtained in the experiments could be directly related to the mass of the analyte. However, a recurring problem in early experiments was the position-dependent sensitivity of the NEMS device. Positional-sensitivity comes about due to the non-uniform vibration profile of the flexural modes in device structures commonly used in NEMS, such as cantilevers or doubly-clamped beams. As the vibration profile, i.e., mode shape, changes along the device, analytes arriving at sensor locations with larger motional amplitude will induce a larger frequency shift than identical analytes arriving at locations with smaller vibration amplitude, e.g., near an anchor point or a node (Ramos et al., 2006, 2007; Stachiv et al., 2012).

Positional sensitivity of different modes was recognized early on with microcantilevers (Dohn et al., 2005; Ghatkesar et al., 2007). Later on, multiple modes were utilized to resolve both mass and

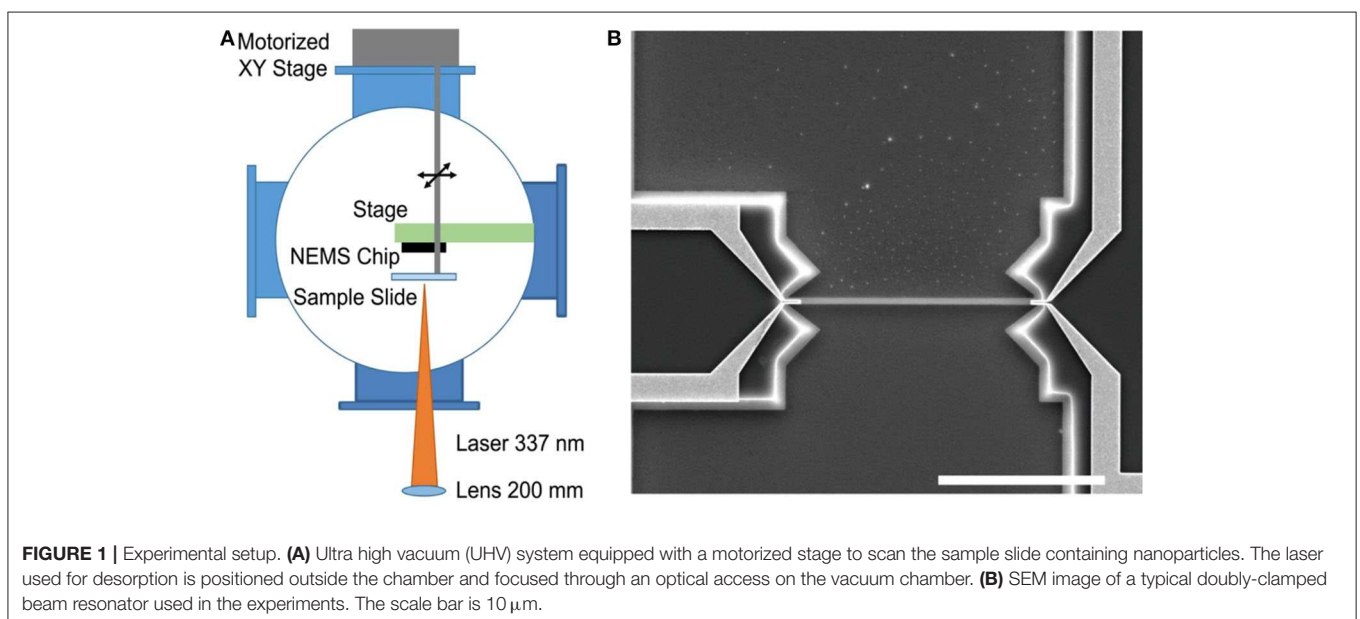
position of the analyte (Dohn et al., 2007, 2010; Naik et al., 2009; Hanay et al., 2012; Bouchaala et al., 2016). The most straightforward way to understand this technique is that there are two unknowns (mass and position), hence two independent equations should be obtained. Frequency measurement in each mode provides one such independent equation. This technique has been colloquially called the *two-mode technique* since the mass of the analyte can be determined if two modes are used in a doubly-clamped beam. In order to utilize this technique several assumptions have to be made. First, the analytes are treated as point masses, mechanical modes are orthogonal to each other and the mode shapes are not affected by particles landed on the beam. Further improvement on the two-mode technique by using even more modes was achieved and mass distribution of the analytes were obtained (Dohn et al., 2010; Biswas et al., 2015; Hanay et al., 2015; Heinrich and Dufour, 2015; Olcum et al., 2015; Sader et al., 2018; Jia and Feng, 2019; Martín-Pérez et al., 2019; Dilena et al., 2020)—an approach called Inertial Imaging. It should be noted that two-mode theory and Inertial Imaging capitalizes on the geometrical diversity of the mode shapes; hence, these ideas can be extended to sensors with distinct mode shapes functioning in other domains. For instance, position sensing of droplets in a microfluidic channel, as well as single cell sensing, have been demonstrated using microwave resonant sensors operated with two modes simultaneously (Kelleci et al., 2018). Another general approach to obtain mass information is to circumvent the issue of position-dependent responsivity altogether by using different device designs (Lobontiu et al., 2006; Park et al., 2010; Sansa et al., 2020).

Although the position information of an analyte plays a critical role in determining the mass, reports on investigating the position-resolution performance of NEMS sensors have been lacking so far. With micro-electromechanical systems and using a gold particle with 0.9 micrometer radius, the relationship between position and modal sensitivity was studied in an

earlier work (Dohn et al., 2007). More recently, the location of cells landing on a microscale mechanical platform was also demonstrated (Malvar et al., 2016) in an experiment where the stiffness of the analyte was also considered in the model. In this work, we took a different approach to obtain a large number of data points to sense single nanoparticles on the NEMS. The experiments were done at room temperature and laser desorption was used to deliver the nanoparticles. The location of each particle was calculated in real-time by the two-mode technique. After each subsequent adsorption of several nanoparticles, the device was removed from the experimental setup for SEM characterization where the locations of the adsorbed nanoparticles are detected individually. The number of detected particles in each cycle was limited to 5 typically (and 20 at most so) to prevent any ambiguity due to crowding while mapping the events detected by NEMS and the particles observed under SEM. This protocol was repeated until sufficient data points were obtained to have a meaningful statistical distribution. We then compared the position measurement results based on mode shapes calculated from different models to determine the accuracy of the detected position of the nanoparticles. For FEM simulations, SiN doubly clamped beam was modeled at two different lengths, 15 and 20  $\mu\text{m}$  and the gold electrodes on top were accounted for in the model as well. The material parameters for standard COMSOL library was used; relevant material parameters are listed in **Table 2**.

## EXPERIMENTAL SETUP

The NEMS chip is positioned in a table-top UHV chamber (Kurt Lesker) where electrical and optical access are provided for transduction of NEMS and desorption of gold nanoparticles, respectively (**Figure 1A**). The experiments are conducted under high vacuum conditions ( $\sim 10^{-8}$  Torr) to reduce molecular interactions and increase the quality factor. The experimental

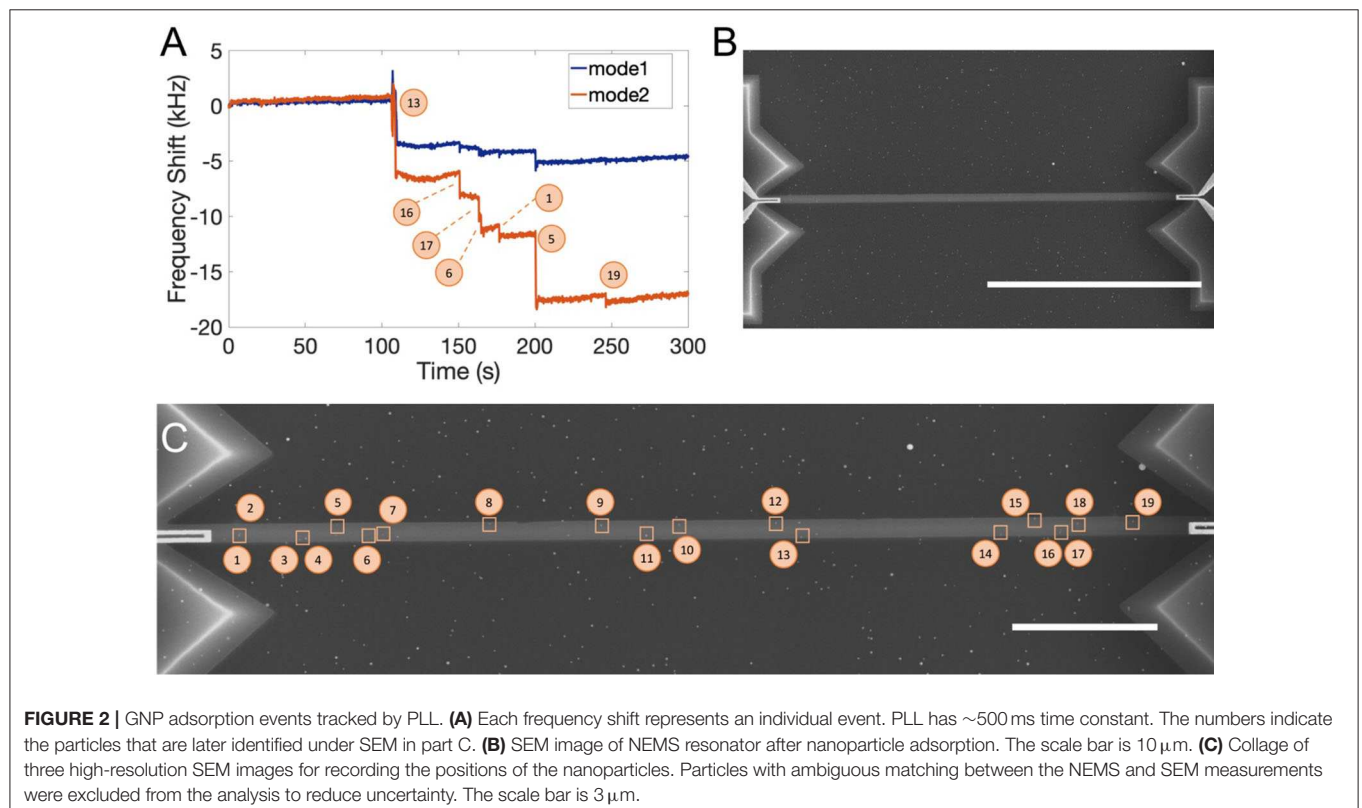


setup for this study is based on an earlier work where backside desorption method was implemented (Yuksel et al., 2019). A nitrogen laser (NL 100, Stanford Research Systems) with the wavelength of 337 nm and energy of 176  $\mu\text{J}$  per pulse is used to perform laser-induced desorption of gold nanoparticles from the surface. Since the laser provides a wide, rectangular beam, focusing is necessary to increase its energy. A lens (with focal distance of 200 mm) is mounted in front of the laser beam shutter and the laser is placed on a manual XYZ positioner in order to align the laser beam with respect to the active area of the NEMS chip. A glass slide containing the analyte molecules can be scanned in-plane using a UHV XY Scanner (Design Multibase, Kurt Lesker). Two stepper motors (McLennan) controlled with

a PIC microcontroller provide the scanning action of the XY stage. A colloidal solution of gold nanoparticles (Sigma Aldrich) with nominal diameter of 20 nm were chosen for this study, since their high density and conductivity render them suitable both for inertial and SEM measurements. After depositing GNP on a glass slide with the help of a micropipette without applying any dilution and waiting for the slide to dry completely (typically 2 h), the glass slide is introduced into an aluminum holder piece inside the chamber. To perform laser-induced desorption, the NEMS chip is mounted on the stage of a flow cryostat (Janis) placed inside the chamber, although the experiments were carried out at room temperature. The glass slide containing the sample is arranged in parallel to the NEMS resonator with the help

**TABLE 1** | Resonance frequencies.

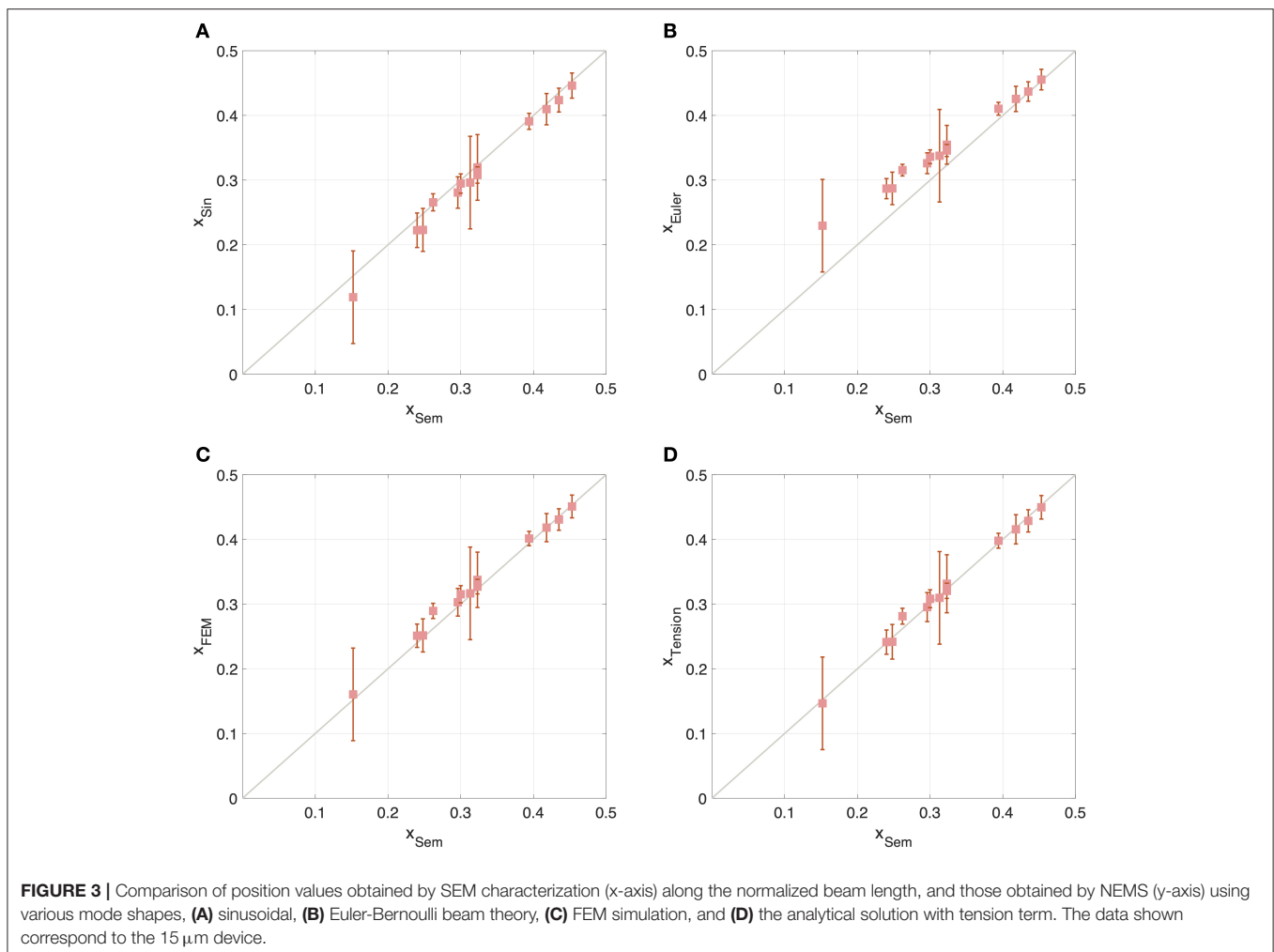
	Beam length ( $\mu\text{m}$ )	$f_1$ (MHz)	$f_2$ (MHz)	Tension value (MPa)	Mode shape data points	Grid points
FEM	15	18.74	38.09	816	2309	1001
	20	13.72	27.69		3052	
Sinusoidal	15	–	–	None	10001	1001
	20	–	–			
Tension	15	18.44	37.49	816	10001	1001
	20	13.553	27.35			
Euler	15	–	–	None	10001	1001
	20	–	–			
Experiment	15	18.76	37.57			
	20	13.72	27.69			

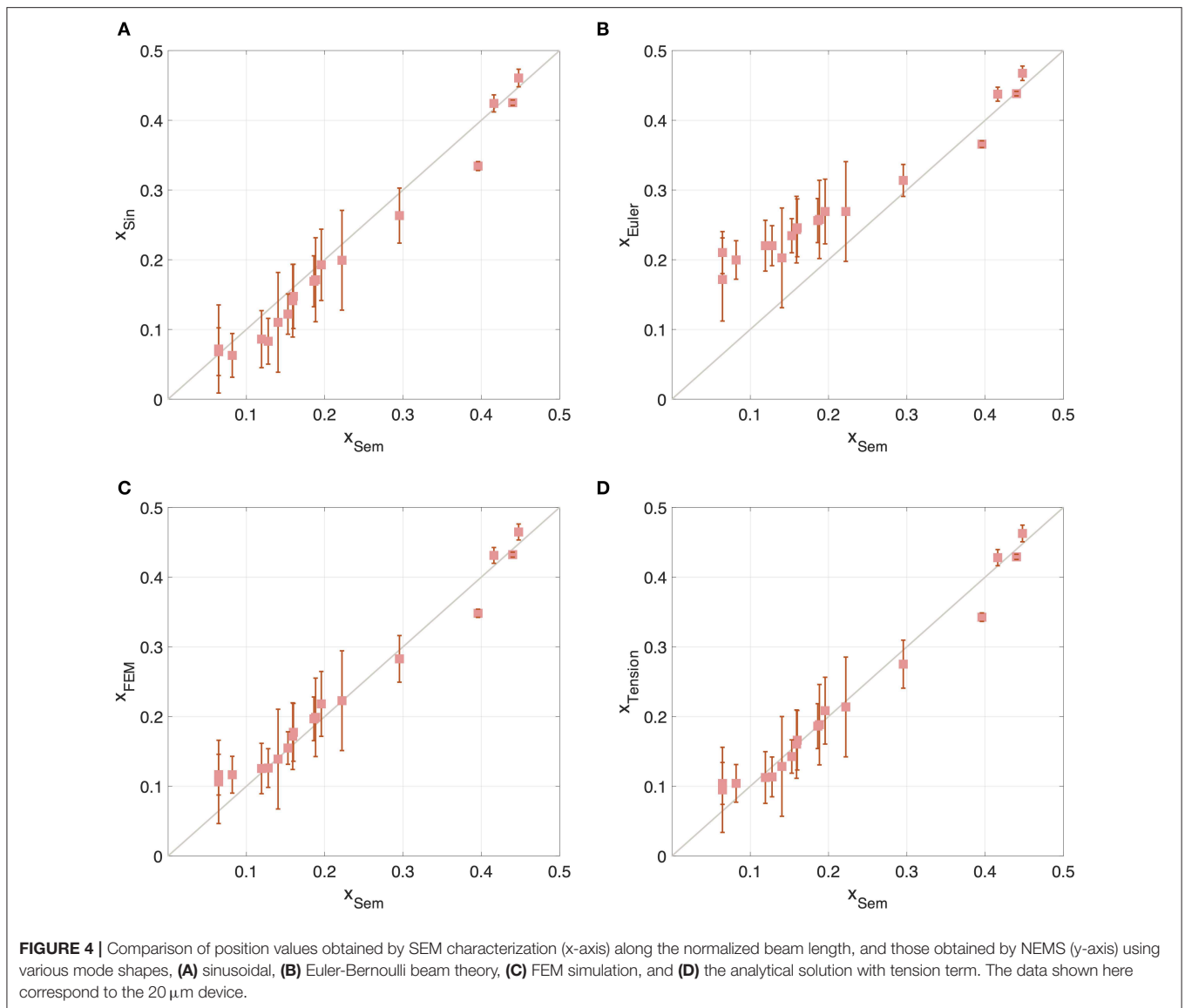


of the holder piece attached on an arm mounted on the XY stage. Systematic scanning of the XY stage is important to span the surface of the glass slide and find the hot spots. Doubly-clamped SiN beam resonators (with large thin-film stress), 15 and 20  $\mu\text{m}$  in length, 370 nm in width and 100 nm in thickness are used in different runs (**Figure 1B**). The fabrication process of the SiN NEMS resonators was reported earlier (Ari et al., 2018). In short, two electron beam lithography steps followed by metal deposition were used to define the gold electrodes and the beam geometry (via a copper etch mask) on a commercial silicon wafer with 100 nm SiN top layer. A succession of anisotropic and isotropic etched, followed by the removal of copper etch mask resulted in the NEMS devices used here. The NEMS resonator is transduced by thermoelastic driving and piezoresistive detection via gold nano-loop electrodes located near both ends of the beam. A.C. voltage at half of the resonance frequency of the beam is applied to the drive port in order to actuate the resonator. Due to the different thermal expansion coefficients of the beam substrate and the electrode (i.e., silicon nitride and gold), thermal stress occurs and exerts a bending moment on the beam. At the same time due to geometric piezoresistivity, resistance of the detection electrode changes with the flexural

motion of the beam, which can be measured by applying an A.C. bias voltage at the resonance frequency (Bargatin et al., 2007; Beardslee et al., 2010; Ari et al., 2018). The resonance frequency values of the NEMS devices are listed in **Table 1**. Allan deviations of  $\sim 1.5 \times 10^{-6}$  are typically obtained for both modes.

To measure the frequency shifts due to the adsorbed analytes, both the first and second modes of the resonator are tracked individually by phase-locked-loops (PLL). A typical time trace of a NEMS nanoparticle sensing experiment is shown in **Figure 2A** where each GNP adsorbed by the sensor induces frequency shifts in two-modes. After collecting several such particles and calculating the positions using the two-mode theory, the NEMS chip is removed for SEM characterization (**Figures 2B,C**). By limiting the number of particles collected for each NEMS/SEM measurement cycle, we minimize the ambiguity in matching the particles between NEMS detection and SEM imaging. Yet, during some NEMS measurements where two particles inevitably land very close to each other resulting in an ambiguous assessment for these particles. Since the current work focuses on the accuracy of position sensing, we did not include any such ambiguous matching events in our analysis. It should be noted that due to





the symmetry of the NEMS and the technique, two particles that land on the two different sides of the beam nearly symmetrically may result in similar position values in NEMS measurements. Moreover, several unmarked nanoparticles in **Figure 2C** have been deposited on the NEMS before the experiments described here started, during a stage where the alignment between the laser-desorption plume and the NEMS chip was being conducted. The NEMS/SEM cycle is repeated until statistically significant number of events are obtained. For the analysis, the SEM results are assumed to be the reference values and any error is calculated accordingly.

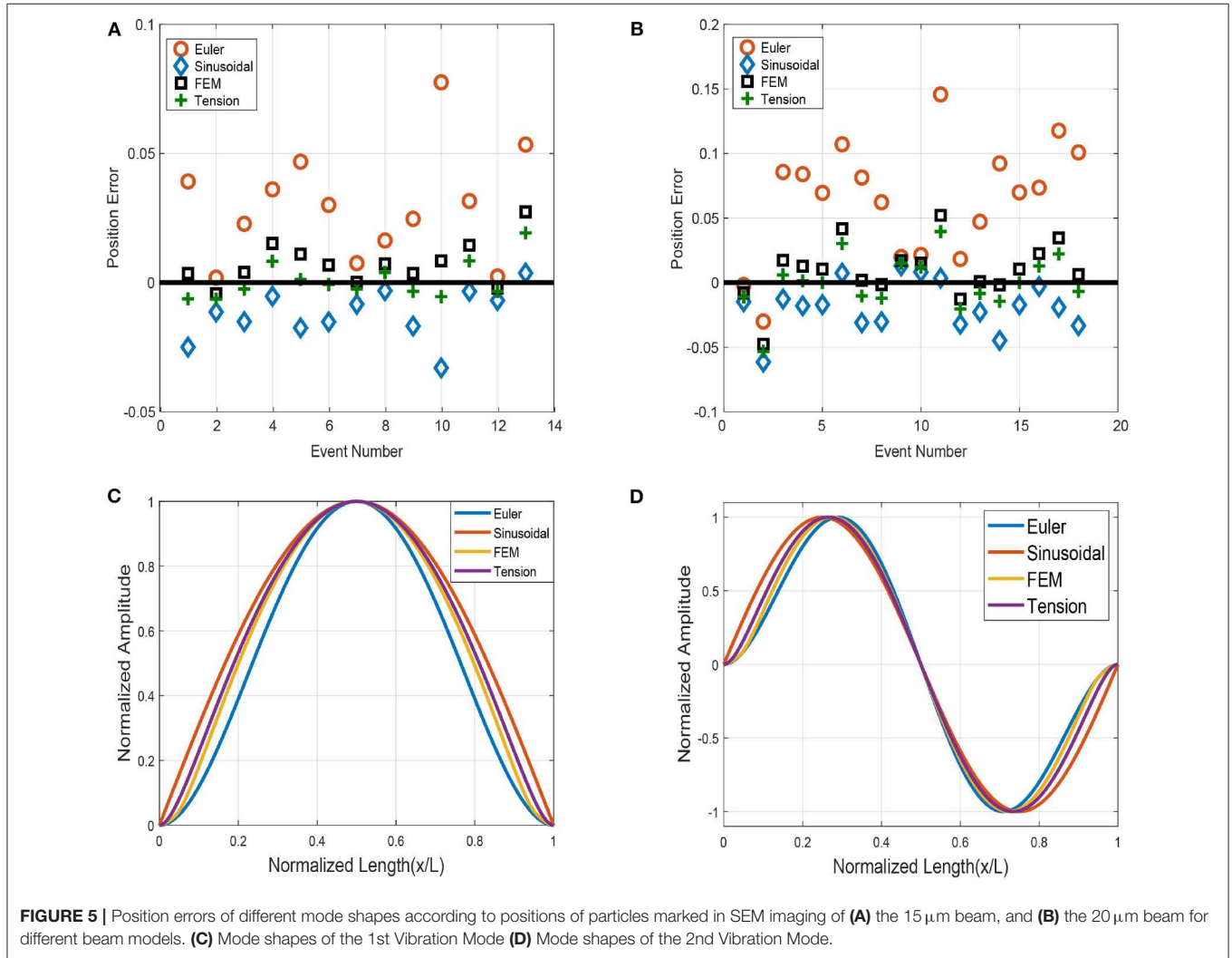
## RESULTS

The comparison between the position values obtained through SEM imaging and frequency shift measurements are shown in **Figures 3, 4** for two resonators with 15 and  $20\ \mu\text{m}$  lengths,

respectively. For each device, different mode shapes for NEMS are used in the analysis. Two of the mode shapes correspond to the two ideal cases, the Euler mode shape for the pure bending solution and the sinusoidal mode shape for the pure string under tension solution (**Supplementary Information**). Of course, the actual NEMS device has elastic contributions from both mechanisms. To calculate the mode shape in this case, we first use the resonance frequency values for the first two modes and FEM analysis to determine the intrinsic stress on the structure (**Table 1**). The stiffness of the beam increases under the existence of intrinsic stress and this increases the resonance frequencies. An axial stress value of 816 MPa is obtained by fitting the resonance frequencies of the first two modes: this stress value agrees with the range of values provided by the supplier of the wafer. Using the stress value, two additional mode shapes are generated (**Table 2** and **Supplementary Information**). The first one uses the combined analytical model of beam bending under

**TABLE 2** | Parameters used in the analytical models and FEM simulations.

Beam	Length( $\mu\text{m}$ )	Width(nm)	Thickness(nm)	Density ( $\text{kg/m}^3$ )	Young's modulus (GPa)	Stress (MPa)
FEM	15/20	370	100	3,100	250	816
Tension	15/20	370	100	3,100	250	816
Sinusoidal	15/20	370	100	3,100	NA	NA
Euler	15/20	370	100	3,100	250	NA



tension (Bokaian, 1990) to generate mode shapes in a MATLAB environment. Finally, mode shapes are directly extracted from the FEM solver using 1001 grid points along the top surface and used to reverse calculate the positions using the two-mode theory. The performance of the two-mode theory with respect to these four different mode shapes is shown in **Figure 5** and tabulated in **Tables 3, 4** for the 15 and 20  $\mu\text{m}$  devices, respectively. We quantify the error by:

$$\text{Position error} \equiv x_{NEMS} - x_{SEM}$$

where we define  $x_{SEM}$  to be the measured position under the SEM (and normalized with respect to the length of the

NEMS), and  $x_{NEMS}$  for the position obtained by converting NEMS frequency shift results into position values by using the corresponding beam model (Euler-Bernoulli, string under tension, beam under tension or mode shapes obtained by FEM).

Mass values of the particles obtained by using analytical solution with tension term are shown in **Tables 3, 4**. The particles that are close to the clamping are excluded since the uncertainty in determining the mass is large in this region. The rms error,  $x_{RMS} = \sqrt{\frac{1}{N} \sum_{n=1}^N |position\ error|^2}$  for each mode shape is tabulated in **Table 5**, where N denotes the number of error values.

**TABLE 3** | Position values for 15  $\mu\text{m}$  beam.

SEM	Sinusoidal	E-B	FEM	Tension
0.248	0.223	0.287	0.252	0.242
0.435	0.424	0.437	0.431	0.429
0.323	0.308	0.346	0.327	0.320
0.300	0.295	0.336	0.315	0.308
0.240	0.222	0.287	0.251	0.241
0.296	0.281	0.326	0.303	0.295
0.418	0.410	0.426	0.418	0.416
0.394	0.391	0.410	0.401	0.398
0.313	0.296	0.338	0.317	0.310
0.152	0.119	0.230	0.160	0.147
0.323	0.320	0.355	0.337	0.331
0.453	0.446	0.455	0.451	0.450
0.262	0.266	0.315	0.289	0.281

**TABLE 4** | Position values for 20  $\mu\text{m}$  beam.

SEM	Sinusoidal	E-B	FEM	Tension
0.440	0.425	0.438	0.432	0.429
0.396	0.334	0.366	0.351	0.343
0.160	0.147	0.246	0.186	0.166
0.159	0.141	0.243	0.181	0.160
0.188	0.171	0.258	0.207	0.188
0.065	0.072	0.172	0.113	0.095
0.153	0.122	0.234	0.165	0.143
0.140	0.110	0.203	0.145	0.128
0.448	0.461	0.467	0.464	0.463
0.416	0.424	0.437	0.431	0.428
0.065	0.068	0.210	0.126	0.104
0.295	0.263	0.314	0.287	0.275
0.222	0.199	0.269	0.228	0.214
0.128	0.083	0.220	0.137	0.113
0.186	0.169	0.256	0.204	0.186
0.196	0.193	0.269	0.225	0.208
0.082	0.063	0.200	0.125	0.104
0.119	0.086	0.220	0.136	0.113

## DISCUSSION

The beam is assumed to have a uniform cross-section, ignoring any fabrication imperfections. Position errors are calculated after matching the SEM positions of the particles with position values obtained from each mode shape. By observing the error trends in **Figure 5**, it is evident that a solution based on pure Euler-Bernoulli (E-B) theory deviates the most from SEM position values presumably due to unaccounted axial stress with this theory. By examining the rms errors in **Table 5**, we see that the remaining three mode shapes yield similar results—the combined analytical mode shape result seems to offer the best performance. This raises a question: how is it that the combined model yields

**TABLE 5** | Rms of errors.

Sinusoidal	Euler	FEM	Tension
<b>15 <math>\mu\text{m}</math> Beam</b>			
0.0154	0.0364	0.0109	0.0072
<b>20 <math>\mu\text{m}</math> Beam</b>			
0.0261	0.0780	0.0235	0.0204

better predictions than the FEM model? The reason is interpreted to be due to the number of grid points in the simulation (1001) along the longitudinal dimension which is a typical value for NEMS simulations. In any case, the results indicate that Euler-Bernoulli mode shapes are not sufficient to accurately determine the position of the analytes when there is significant stress on the beam.

Another important trend in **Figures 3, 4** is that the two-mode theory works much better near the center of the beam and the accuracy near the center is relatively insensitive to the model selected. This trend is expected due to the increased sensitivity away from the clamps, especially for the first mode. As it is seen in **Figure 5**, mode shapes of FEM model and analytical solution with tension term show similar trend and sinusoidal mode shape is even closer to them than the Euler-Bernoulli mode shape. It demonstrates that the sinusoidal model can serve as a starting model for position sensing, and that the tension or FEM models are more accurate when the particles are landing away from the center of the beam.

Both the stress and the bending rigidity play an important role in the mode shapes of the NEMS devices. On the other hand, the sinusoidal and the Euler-Bernoulli mode shapes are merely the two limiting cases for the beam model: zero bending rigidity and zero stress, respectively. Since the actual mode shapes are in between these two limiting factors, the predictions of the sinusoidal and EB mode shapes err in opposite directions. The prediction error of the sinusoidal and EB mode shapes are the largest for particles landing near the edges and they are indicative of the distinct boundary conditions imposed by the underlying dynamics assumed for each case: pinned-pinned boundary conditions for the sinusoidal, and clamped-clamped boundary conditions for the EB mode shapes. Near the center of the beam, the effects of the boundary conditions are washed out, and the beam equations of different models are sufficiently similar to each other to give rise to a convergence of mode shapes and predictions of particle positions.

The function which is defined as the ratio of the first mode shape to the second mode shape is the identifying factor to determine the landing position (Hanay et al., 2012). The models used to calculate the mode shapes show slightly different results from each other, therefore results in different ratios. For example, the slope of the first two mode shapes vanishes on the clamped edges in the Euler-Bernoulli model while it has a finite value in the string-under-tension model. In reality, the mode shapes are expected to lie between these two extremes, therefore the ratio of the mode shapes will have a value in between. The particular geometry of the mode shapes in each

model will determine whether the model will under-estimate or over-estimate the position.

Any improvement in the determination of the position of a particle is expected to increase the accuracy of the mass measurement of that particle. This statement can be understood by considering the equation that relates the mass and position of a point particle written for the fundamental mode as (Hanay et al., 2012):

$$\Delta m = -2M_{eff} \left( \frac{\Delta f}{f_0} \right) \frac{1}{\phi(x)^2}$$

where  $\Delta m$  is the mass and  $x$  is the position of the particle;  $M_{eff}$  is the effective mass,  $\Delta f$  is the frequency shift,  $f_0$  is the resonance frequency, and  $\phi(x)$  is the mode shape of the fundamental mode [normalized such that  $\max(\phi(x)) = 1$ ]. Since there is a direct correspondence between the mass and the position of the particle, one can then use standard techniques for error propagation to relate the uncertainty in one parameter to the other (Hanay et al., 2012).

The experimentally determined mean diameter of nanoparticles is 36.5 nm and the mean mass value is 297 MDa which indicates a significant amount of aggregation of nanoparticles. Nevertheless, the position analysis conducted here does not directly depend on the specific mass value of the analytes, since the position value depends on the ratio of the frequency shift in the second mode to the frequency shift in the first mode—and this ratio is constant to first order for particles of different mass but the same position. It would have been interesting to compare the mass spectrum of nanoparticles calculated by using the position values of different models. However, this comparison cannot be properly made for the GNP sample used, because of the high dispersion of the molecular weight (~40%) and the aggregation of nanoparticles during the sample preparation.

## CONCLUSION

We investigated the position sensing performance of NEMS sensors by calculating the position values for multiple GNPs using different models of beam elasticity. Independent SEM characterization of each adsorption was used to validate GNP positions. The analysis suggests tension term should be included to the beam theory for the mode shape calculations especially for structures under high tensile stress. Moreover, the performance of mode shapes obtained by either a simple sinusoidal approximation or through FEM analysis resulted in acceptable performance levels for the determination of particle

## REFERENCES

Ahmad, M. R., Nakajima, M., Kojima, S., Homma, M., and Fukuda, T. (2011). Buckling nanoneedle for characterizing single cells mechanics inside environmental SEM. *IEEE Trans. Nanotechnol.* 10, 226–236. doi: 10.1109/TNANO.2009.2036997

positions. Meticulous measurements of device dimensions after fabrication under the SEM followed by FEM modeling is one possible approach to increase position resolution. Keeping a record of particles as they land on the sensor and using this information to update the mode shape using perturbation theory (Yüksel and Hanay, 2017) can also alleviate uncertainties due to mode shape. The accuracy of mode shapes is crucial in position-dependent sensing applications. Since nanomechanical motion occurs at high frequencies and on a miniscule area, it is challenging to image the actual mode shape. However, using SEM and averaging of the resonant motion (Ghatkesar et al., 2007), or imaging post-buckling curves can be used to capture the effective mode shape (Ahmad et al., 2011; Erbil et al., 2020). The use of correct mode shapes increases the position sensing performance of nanomechanical sensors which can then enable the delivery, positioning, and control of nanoparticles within the NEMS platform.

## DATA AVAILABILITY STATEMENT

The datasets generated for this study are available on request to the corresponding author.

## AUTHOR CONTRIBUTIONS

MH, EO, and MY conceived the idea. EO, MY, and UH designed the experimental setup. CY, AA, AY, and EO fabricated the devices. EO and MY acquired the data and performed the analyses. All authors contributed in writing the manuscript.

## FUNDING

This work was funded by the Scientific and Technological Research Council of Turkey (TÜBİTAK), Grant No. EEEAG-115E230.

## ACKNOWLEDGMENTS

MH acknowledges the Science Academy, Turkey (Bilim Akademisi) and the Turkey Academy of Sciences (TÜBA) for support.

## SUPPLEMENTARY MATERIAL

The Supplementary Material for this article can be found online at: <https://www.frontiersin.org/articles/10.3389/fmech.2020.00037/full#supplementary-material>

Ari, A. B., Karakan, M. Ç., Yanik, C., Kaya, I. I., and Hanay, M. S. (2018). Intermodal coupling as a probe for detecting nanomechanical modes. *Phys. Rev. Appl.* 9:034024. doi: 10.1103/PhysRevApplied.9.034024

Bargatin, I., Kozinsky, I., and Roukes, M. L. (2007). Efficient electrothermal actuation of multiple modes of high-frequency nanoelectromechanical resonators. *Appl. Phys. Lett.* 90, 093116. doi: 10.1063/1.2709620

- Beardslee, L. A., Addous, A. M., Heinrich, S., Josse, F., Dufour, I., and Brand, O. (2010). Thermal excitation and piezoresistive detection of cantilever in-plane resonance modes for sensing applications. *J. Microelectromech. Syst.* 19, 1015–1017. doi: 10.1109/JMEMS.2010.2052093
- Biswas, T., Xu, J., Miriyala, N., Doolin, C., Thundat, T., Davis, J., et al. (2015). Time-resolved mass sensing of a molecular adsorbate nonuniformly distributed along a nanomechanical string. *Phys. Rev. Appl.* 3:064002. doi: 10.1103/PhysRevApplied.3.064002
- Bokaian, A. (1990). Natural frequencies of beams under tensile axial loads. *J. Sound Vib.* 142, 481–498. doi: 10.1016/0022-460X(90)90663-K
- Bouchaala, A., Nayfeh, A. H., Jaber, N., and Younis, M. I. (2016). Mass and position determination in MEMS mass sensors: a theoretical and an experimental investigation. *J. Micromech. Microeng.* 26:105009. doi: 10.1088/0960-1317/26/10/105009
- Chaste, J., Eichler, A., Moser, J., Ceballos, G., Rurali, R., and Bachtold, A. (2012). A nanomechanical mass sensor with yoctogram resolution. *Nat. Nanotechnol.* 7:301. doi: 10.1038/nnano.2012.42
- Chiu, H.-Y., Hung, P., Postma, H. W. C., and Bockrath, M. (2008). Atomic-scale mass sensing using carbon nanotube resonators. *Nano Lett.* 8, 4342–4346. doi: 10.1021/nl802181c
- Dilena, M., Dell'oste, M. F., Fernández-Sáez, J., Morassi, A., and Zaera, R. (2020). Hearing distributed mass in nanobeam resonators. *Int. J. Solids Struct.* 183–194, 568–592. doi: 10.1016/j.ijsolstr.2020.02.025
- Dohn, S., Sandberg, R., Svendsen, W., and Boisen, A. (2005). Enhanced functionality of cantilever based mass sensors using higher modes. *Appl. Phys. Lett.* 86:233501. doi: 10.1063/1.1948521
- Dohn, S., Schmid, S., Amiot, F., and Boisen, A. (2010). Position and mass determination of multiple particles using cantilever based mass sensors. *Appl. Phys. Lett.* 97:044103. doi: 10.1063/1.3473761
- Dohn, S., Svendsen, W., Boisen, A., and Hansen, O. (2007). Mass and position determination of attached particles on cantilever based mass sensors. *Rev. Sci. Instrum.* 78:103303. doi: 10.1063/1.2804074
- Ekinci, K. L., Huang, X. M. H., and Roukes, M. L. (2004a). Ultrasensitive nanoelectromechanical mass detection. *Appl. Phys. Lett.* 84, 4469–4471. doi: 10.1063/1.1755417
- Ekinci, K. L., Yang, Y. T., and Roukes, M. L. (2004b). Ultimate limits to inertial mass sensing based upon nanoelectromechanical systems. *J. Appl. Phys.* 95, 2682–2689. doi: 10.1063/1.1642738
- Erbil, S., Hatipoglu, U., Yanik, C., Ghavami, M., Ari, A., Yuksel, M., et al. (2020). Full electrostatic control of nanomechanical buckling. *Phys. Rev. Lett.* 124:046101. doi: 10.1103/PhysRevLett.124.046101
- Ghatkesar, M. K., Barwich, V., Braun, T., Ramseyer, J.-P., Gerber, C., Hegner, M., et al. (2007). Higher modes of vibration increase mass sensitivity in nanomechanical microcantilevers. *Nanotechnology* 18:445502. doi: 10.1088/0957-4484/18/44/445502
- Hanay, M. S., Kelber, S., Naik, A. K., Chi, D., Hentz, S., Bullard, E. C., et al. (2012). Single-protein nanomechanical mass spectrometry in real time. *Nat. Nanotechnol.* 7, 602–608. doi: 10.1038/nnano.2012.119
- Hanay, M. S., Kelber, S. I., O'connell, C. D., Mulvaney, P., Sader, J. E., and Roukes, M. L. (2015). Inertial imaging with nanomechanical systems. *Nat. Nanotechnol.* 10, 339–344. doi: 10.1038/nnano.2015.32
- Heinrich, S. M., and Dufour, I. (2015). Toward higher-order mass detection: Influence of an adsorbate's rotational inertia and eccentricity on the resonant response of a Bernoulli-Euler cantilever beam. *Sensors* 15, 29209–29232. doi: 10.3390/s151129209
- Ilic, B., Craighead, H. G., Krylov, S., Senaratne, W., Ober, C., and Neuzil, P. (2004). Attogram detection using nanoelectromechanical oscillators. *J. Appl. Phys.* 95, 3694–3703. doi: 10.1063/1.1650542
- Jensen, K., Kim, K., and Zettl, A. (2008). An atomic-resolution nanomechanical mass sensor. *Nat. Nanotechnol.* 3, 533. doi: 10.1038/nnano.2008.200
- Jia, H., and Feng, P. X.-L. (2019). Very high-frequency silicon carbide microdisk resonators with multimode responses in water for particle sensing. *J. Microelectromech. Syst.* 28, 941–953. doi: 10.1109/JMEMS.2019.2920329
- Kelleci, M., Aydogmus, H., Aslanbas, L., Erbil, S. O., and Hanay, M. S. (2018). Towards microwave imaging of cells. *Lab Chip* 18, 463–472. doi: 10.1039/C7LC01251A
- Lassagne, B., Garcia-Sanchez, D., Aguasca, A., and Bachtold, A. (2008). Ultrasensitive mass sensing with a nanotube electromechanical resonator. *Nano Lett.* 8, 3735–3738. doi: 10.1021/nl801982v
- Lobontiu, N., Ilic, B., Garcia, E., Reissman, T., and Craighead, H. (2006). Modeling of nanofabricated paddle bridges for resonant mass sensing. *Rev. Sci. Instrum.* 77:073301. doi: 10.1063/1.2221560
- Malvar, O., Ruz, J., Kosaka, P. M., Domínguez, C. M., Gil-Santos, E., Calleja, M., et al. (2016). Mass and stiffness spectrometry of nanoparticles and whole intact bacteria by multimode nanomechanical resonators. *Nat. Commun.* 7:13452. doi: 10.1038/ncomms13452
- Martín-Pérez, A., Ramos, D., Gil-Santos, E., García-López, S., Yubero, M. L., Kosaka, P. M., et al. (2019). Mechano-optical analysis of single cells with transparent microcapillary resonators. *ACS Sens.* 4, 3325–3332. doi: 10.1021/acssensors.9b02038
- Naik, A. K., Hanay, M. S., Hiebert, W. K., Feng, X. L., and Roukes, M. L. (2009). Towards single-molecule nanomechanical mass spectrometry. *Nat. Nanotechnol.* 4, 445–450. doi: 10.1038/nnano.2009.152
- Olcum, S., Cermak, N., Wasserman, S. C., and Manalis, S. R. (2015). High-speed multiple-mode mass-sensing resolves dynamic nanoscale mass distributions. *Nat. Commun.* 6:7070. doi: 10.1038/ncomms8070
- Park, K., Millet, L. J., Kim, N., Li, H., Jin, X., Popescu, G., et al. (2010). Measurement of adherent cell mass and growth. *Proc. Natl Acad. Sci. U.S.A.* 107, 20691–20696. doi: 10.1073/pnas.1011365107
- Ramos, D., Calleja, M., Mertens, J., Zaballós, Á., and Tamayo, J. (2007). Measurement of the mass and rigidity of adsorbates on a microcantilever sensor. *Sensors* 7, 1834–1845. doi: 10.3390/s7091834
- Ramos, D., Tamayo, J., Mertens, J., Calleja, M., and Zaballós, A. (2006). Origin of the response of nanomechanical resonators to bacteria adsorption. *J. Appl. Phys.* 100:106105. doi: 10.1063/1.2370507
- Sader, J. E., Hanay, M. S., Neumann, A. P., and Roukes, M. L. (2018). Mass spectrometry using nanomechanical systems: beyond the point-mass approximation. *Nano Lett.* 18, 1608–1614. doi: 10.1021/acs.nanolett.7b04301
- Sansa, M., Defoort, M., Brenac, A., Hermouet, M., Banniard, L., Fafin, A., et al. (2020). Optomechanical mass spectrometry. *arXiv preprint arXiv:2004.06683*.
- Stachiv, I., Fedorchenko, A., and Chen, Y.-L. (2012). Mass detection by means of the vibrating nanomechanical resonators. *Appl. Phys. Lett.* 100:093110. doi: 10.1063/1.3691195
- Tamayo, J., Ramos, D., Mertens, J., and Calleja, M. (2006). Effect of the adsorbate stiffness on the resonance response of microcantilever sensors. *Appl. Phys. Lett.* 89:224104. doi: 10.1063/1.2388925
- Yang, Y. T., Callegari, C., Feng, X. L., Ekinci, K. L., and Roukes, M. L. (2006). Zeptogram-scale nanomechanical mass sensing. *Nano Lett.* 6, 583–586. doi: 10.1021/nl052134m
- Yuksel, M., and Hanay, M. S. (2017). Mode-shape perturbation induced by analyte adsorption in nanomechanical sensors. *arXiv* 1709:01496.
- Yuksel, M., Orhan, E., Yanik, C., Ari, A. B., Demir, A., and Hanay, M. S. (2019). Nonlinear nanomechanical mass spectrometry at the single-nanoparticle level. *Nano Lett.* 19:b00546. doi: 10.1021/acs.nanolett.9b00546

**Conflict of Interest:** The authors declare that the research was conducted in the absence of any commercial or financial relationships that could be construed as a potential conflict of interest.

Copyright © 2020 Orhan, Yuksel, Ari, Yanik, Hatipoglu, Yağci and Hanay. This is an open-access article distributed under the terms of the Creative Commons Attribution License (CC BY). The use, distribution or reproduction in other forums is permitted, provided the original author(s) and the copyright owner(s) are credited and that the original publication in this journal is cited, in accordance with accepted academic practice. No use, distribution or reproduction is permitted which does not comply with these terms.